Progress in Photovoltaics: Research and Applications

WILEY

PROGRESS IN PHOTOVOLTAICS

RESEARCH ARTICLE OPEN ACCESS

Optimizing Na and Rb Incorporation Along With Bandgap Grading for High Efficiency Ultra-Thin CIGSe Solar Cells

Christoph Rath | Tristan Köhler | Martina Schmid

Faculty of Physics and CENIDE, University of Duisburg-Essen, Duisburg, Germany

Correspondence: Christoph Rath (christoph.rath@uni-due.de)

Received: 26 November 2025 | **Revised:** 13 April 2026 | **Accepted:** 21 May 2026

ABSTRACT

This work investigates the role of Na and Rb incorporation in ultra-thin Cu(In,Ga)Se_2 (CIGSe) solar cells, focusing on performance optimization. By systematically varying the Rb content and combining predeposited Na with postdeposited Rb, we identify the optimal configuration, achieving efficiencies of 11.72% on Mo and 10.48% on ITO. Comprehensive structural and electrical characterization reveals that Rb not only enhances the absorber quality through superior grain boundary passivation, following a Na–Rb exchange mechanism, but also modifies the CIGSe/CdS interface by influencing the absorber surface and Cd incorporation. While combined Na and Rb postdeposition treatments suppress Cd incorporation, predeposited Na can promote it. In both cases, the added Na and Rb support the creation of an ordered vacancy compound (OVC) layer, which improves the band alignment. Temperature-dependent IV (IVT) measurements distinguish between interface and bulk recombination, revealing a Schottky barrier originating from possible GaO_x formation at the ITO/CIGSe interface, as well as a current-blocking behavior at the CIGSe/CdS interface at low temperatures related to Rb. Tuning the Ga distribution further enhances device performance: An In-Ga-In sequence in the first stage of absorber growth suppresses Rb/CdS-related barriers and further promotes alkali metal incorporation, supporting OVC layer growth and thereby possibly improving band alignment. A mechanistic model showcasing this interplay between Na, Rb, OVC, and Cd is made for visualizing the structural formation during absorber growth. These results underline the relevance of the first systematic Rb analysis in ultra-thin CIGSe solar cells and highlight the synergistic potential of combining alkali metal doping with Ga grading to improve ultra-thin CIGSe solar cells.

1 | Introduction

The increasing global energy demand, coupled with rising emissions and climate-related catastrophes, increases the demand for renewable energies. Thin-film solar cells broaden the scope of photovoltaics by serving applications in which they outperform conventional cells. The advantage of thin-film solar cells is firstly that, due to their direct band gap, significantly less absorber material is required, and they are thus less dependent on critical metals while maintaining a high efficiency. Secondly, their flexibility and low weight make them suitable for curved and weight-restricted surfaces, as well as for installations that do not allow for complex support structures. Thirdly, when deposited on a transparent back contact, light management enables tailored light distribution between absorption and transmission, compensating for reduced thicknesses and opening up applications in tandems, agrivoltaics, or building-integrated photovoltaics [1].

Cu(In,Ga)Se_2 (CIGSe) solar cells are a subtype of thin- or even ultra-thin solar cells. They show promise because of their possible flexibility, lightweight nature, along with a tunable bandgap, making them optimal for semitransparent and building-integrated solar cells. Additionally, the potential for further increase in electrical performance, for example, by optimized alkali treatment or bandgap grading, will make CIGSe solar cells play a key role in the future solar industry.

J. Hedstrom et al. discovered in 1993 that alkali elements have a positive effect on the overall efficiency of CIGSe solar cells. In these investigations, Na diffused from soda-lime-glass into the absorber [2]. Since then, besides the lightweight alkali elements, heavy alkali elements have also been incorporated into the absorber and researched. The current world record of a CIGSe solar cell with an efficiency of 23.64%, presented by J. Keller et al. [3], utilizes an optimized Na and Rb treatment.

The positive effect of Na at low concentration in the CIGSe absorber is explained by three main reasons. Firstly, it accumulates at grain boundaries [4] where it not only passivates them but also acts as a Se reservoir in the form of $Na_{2-x}Se$, making more Se available during the growth phase [5]. Na can furthermore diffuse into the grain interior because of Cu vacancies V_{Cu} as Na(In, Ga)Se_2 (Na_{Cu}). When the absorber is cooling down, the Na loses its thermodynamic stability [6, 7], causing the Na to diffuse out of the Na_{Cu} and leaving behind a $V_{Cu,}$ which increases the beneficial p-type defects in the absorber.

Moreover, Na can suppress defects as shown by S. Wei et al. [7] such as In_{Cu} by forming Na_{Cu}. In the CIGSe absorber, In_{Cu} acts as a donor and thus reduces the p-type carrier concentration. Therefore, suppressing these In_{Cu} defects by Na allows for a further increase in p-type carrier concentration. All these effects are present for predeposited Na, whereas when postdepositing Na, the main effect is grain boundary passivation [8].

There has been no observation so far that Rb incorporates itself into the grain interior other than a $RbInSe_2$ (RISe) layer. It generally accumulates at the front and rear of the absorber and at the grain boundaries [3]. If Rb is evaporated after Na has been incorporated, an exchange mechanism is observed, meaning that Rb pushes the Na away from the grain boundaries, partially into the grain interior, and partially out of the absorber [6]. This conclusion was made since the concentration of Na in the grain interior increases after RbF treatment [9]. Because of this exchange mechanism, the effect of the in and out diffusion of Na is enhanced, while the effect of grain boundary passivation by Rb is superior to Na passivation [10]. As a result, the effect of Na is boosted, increasing the p-type carrier concentration. Furthermore, recombination losses are decreased because of superior grain passivation by Rb.

Rb has similar effects as Na on the doping qualities of the absorber and can increase the open-circuit voltage V_{oc} with little effect on the short-circuit current density J_{sc} [11]. There have been several studies regarding the formation of RISe, stating that a RISe layer is forming on top of the absorber [12], only RISe-point contacts are forming [11, 13], or that RISe is not forming at all [14]. In the case of ultra-thin CIGSe, it is realistic to assume that point contacts are forming on the surface since less Rb is expected to be used in comparison to thin-film studies.

The RISe layer is an n-type material with a bandgap of $E_g = 2.0–2.57$ eV [14]. A favorable impact on band alignment between CIGSe with a bandgap of $E_g = 1.04–1.68$ eV [15] and CdS with $E_g = 2.5$ eV [16] results, as RISe falls right within that range. A subsequently reduced energy barrier for electrons implies reduced recombination at the CIGSe/CdS interface.

D. Kim et al. [1], M. Saifullah et al. [17], and Y. Li et al. [18] optimized the Na incorporation in ultra-thin CIGSe solar cells and performed detailed electrical and optical investigations. However, no such analysis was found for Rb. This raises the question of how the additional incorporation of Rb impacts the performance of ultra-thin CIGSe. It remains to be proven that it boosts the performance in the same way as it was observed for 2-μm-thick CIGSe absorbers.

Through structural, compositional, and detailed opto-electronic characterization of solar cells with different Rb amounts evaporated onto the absorber, the impact of Rb on ultra-thin CIGSe will be analyzed.

2 | Experimental

The substrates are ≈800-nm-thick Mo layers on SLG substrates with a Na diffusion barrier or 400-nm-thick ITO sputtered on Na-poor glass so that the Na incorporation can be limited and controlled. The ultra-thin (≈500 nm) CIGSe absorbers are evaporated on the substrates by using physical vapor deposition (PVD) in a three-stage co-evaporation process, which is monitored by a laser light scattering (LLS) signal. During all stages, Se is evaporated at 255°C to maintain a constant Se atmosphere. In the first stage, In and Ga are evaporated on the substrate sequentially, with a substrate temperature of 410°C to define the absorber's gradient. The standard sequence, Ga followed by In (named GaIn), produces a single grading, while an alternative sequence, In ➔ Ga ➔ In (named InGaIn), is tested to achieve a double grading, with the same [Ga]/([Ga] + [In]) ratio (GGI) and overall thickness. In the second stage, Cu is evaporated at a substrate temperature of 450°C until the [Cu]/([Ga] + [In]) ratio (CGI) has reached 1.05, which is observed with the help of the stoichiometric point. In the third stage, In and Ga are evaporated simultaneously, until a GGI of 0.9 is reached, during which the substrate is cooled down to 410°C again.

After these three stages, the samples are selenized for another 20 min. During this time, Na and Rb are postdeposited (PDT) after the formation of the absorber. Na can additionally be used as a predeposition treatment (pre-DT) before the formation of the absorber. In every process involving Na PDT, Na is evaporated first, followed by Rb. The Na source is set to 900°C during evaporation, and the Rb source is first set to 625°C for 5 min and then ramped up to 700°C to ensure all of the Rb is evaporated.

Onto the finished absorber layer, a 50- to 80-nm-thick CdS buffer layer is deposited via chemical bath deposition (CBD). The front contact consists of sputtered i-ZnO (80 nm) and Al:ZnO (300 nm). The solar cell is finished with 2-μm-thick Ni/Al front contacts. Afterwards, eight solar cells with an active area of 0.5 cm^2 are defined by mechanical scribing.

The naming of the variations used in the following explains how much Na and Rb are applied. For example, the Na2Rb4 variation has 2 mg of Na and 4 mg of Rb, both applied by PDT. The sample preNa2Rb6 has 2 mg of predeposited Na paired with 6 mg of Rb PDT. About 2 mg is chosen because for the same PVD used in this work, Y. Li determined it to be the optimal amount for ultra-thin CIGSe absorbers [18].

To identify the absorber thickness and composition after the three-stage co-evaporation, X-ray fluorescence (XRF) spectroscopy was used. Glow-discharge optical emission spectroscopy (GDOES) provided the depth-dependent elemental distribution on completed solar cells. Owing to the lack of absolute calibration for molar concentrations, the GDOES data are utilized here to identify relative trends and compositional shifts. External quantum efficiency (EQE) was measured using a lock-in amplifier in combination with a monochromator, and a calibrated Si and Ge photodiode as reference, covering a spectral range from 300 to 1350 nm. Current–voltage (IV) characteristics were measured under standard test conditions (25°C, AM1.5 spectrum, 1000 W/m^2). Temperature-dependent IV (IVT) measurements were performed in a vacuum-sealed cryostat over a range of 170–300 K, with a temperature sensor positioned next to the solar cell and illumination times up to 10 s. Light intensity-dependent IV measurements (IVC) were conducted with light intensity ranging from 0.3 to 2 suns at room temperature (1 sun = 100 mW/cm^2).

3 | Results and Discussion

3.1 | Variation of Rb Amount for Fixed Na Content

In Table 1, the absorber thickness, the CGI, and the GGI ratio are shown as determined by XRF before CdS deposition and averaged over at least three samples for each variation.

All absorbers are ultra-thin (< 500 nm) with stable CGI of ≈0.9 and GGI ≈0.3, providing good comparability. Differences in absorber thickness may cause slight deviations in electrical data, but the effect of alkali metal doping is expected to dominate.

GDOES gives us information about the elemental depth distribution and was measured on finished solar cells. The GDOES measurement provides only the estimated depth for all elements of interest. Thus, the absorbers are compared across the relative depth, which is taken from the maximum Cd concentration until 50% Mo-concentration is reached. In Figure 1a, the derived GGI can be seen with the bandgap variation above, extracted through the In and Ga molar concentration of the GDOES measurement. The bandgap E_g can be calculated via [19]

$$E_g = \left(1.00 + 0.13\,x^2 + 0.55\,x\right)\ \text{eV}$$

TABLE 1 | X-ray fluorescence (XRF) data of ultra-thin CIGSe solar cells with different alkali treatments.

Sample	Absorber thickness (nm)	CGI	GGI
Na2Rb0	494 ± 7.28	0.876 ± 0.015	0.312 ± 0.004
Na2Rb2	461.66 ± 4.51	0.887 ± 0.015	0.297 ± 0.006
Na2Rb4	470.33 ± 13.01	0.900 ± 0.020	0.303 ± 0.006
Na2Rb6	489.33 ± 8.74	0.897 ± 0.006	0.313 ± 0.006
Na2Rb8	493 ± 9.54	0.937 ± 0.021	0.313 ± 0.006
preNa2Rb6	481 ± 8.86	0.894 ± 0.025	0.316 ± 0.006

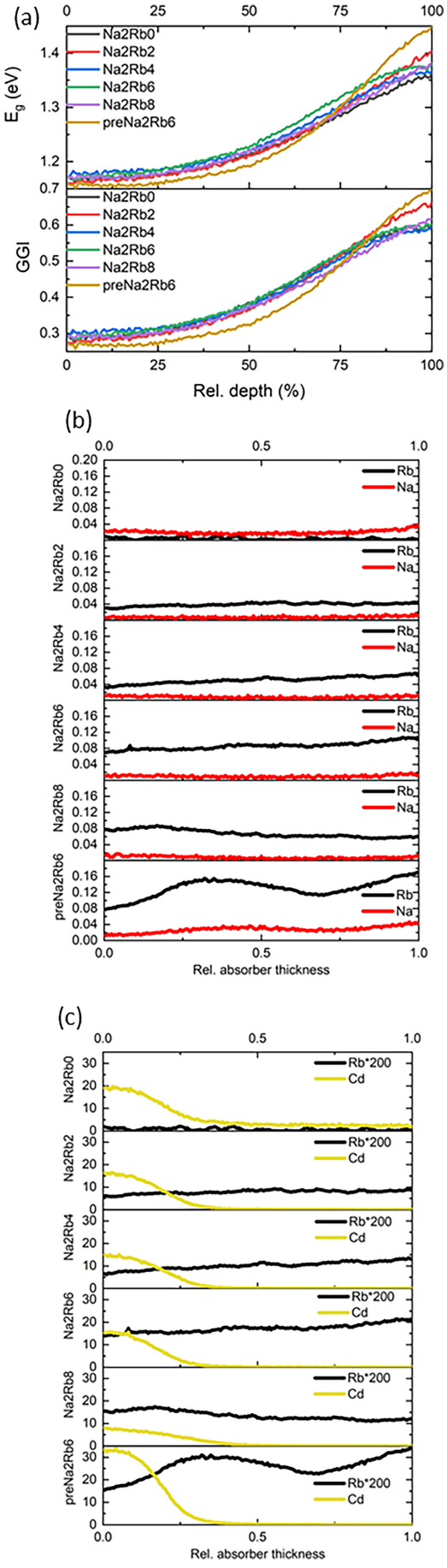

FIGURE 1 | Legend on next page.

FIGURE 1 | (a) GGI measured by GDOES and bandgap E_g extracted therefrom. (b) Depth-dependent molar concentrations of Na and Rb. (c) Depth-dependent molar concentrations of Rb and Cd, for different alkali metal-treated ultra-thin CIGSe solar cells.

with *x* being the GGI. The GGI shows no significant differences between Na2Rb0, ..., Na2Rb8. Only for preNa2Rb6, a steeper gradient is observed. Na acts as a reservoir for Se in the form of $Na_{2-x}Se$ [20] supporting the growth of CIGSe grains. If Na is already present during grain growth, the grains can form faster, and the interdiffusion between In and Ga is reduced, making the gradient steeper. In Figure 1b, the molar concentrations of Na and Rb are compared. The Na concentration is decreasing for variations containing an increasing amount of Rb (Na2Rb2 to Na2Rb8). The Rb signal for the variation Na2Rb0 is noise from the measurement since no Rb was applied. Furthermore, the molar concentration of Rb does not increase linearly. When doubling the amount of Rb from variation Na2Rb2 to Na2Rb4, the molar concentration does not double. A similar behavior can be observed when comparing variations Na2Rb6 and Na2Rb8.

The declining Na level strengthens the argument for the exchange mechanism between Na and Rb, though it cannot be said if the Na is pushed into the grain interior. It can only be stated that the Rb interacts with the Na by pushing it out of the absorber because of the lower Na concentration in the absorber after the Rb PDT has been applied.

The Rb content is almost the same for Na2Rb6 and Na2Rb8, but its slope is inverted, indicating that for Na2Rb8, most Rb is at the front side of the absorber. During the CBD of the CdS buffer layer, a significant amount of residual Rb is washed away, leading to the reduced amount of Rb for Na2Rb8. T. Kodalle speculated that an NH_3-soluble Rb-component forms at the surface of the CIGSe absorber after Rb PDT [9]. J. Keller et al. observed the same behavior on AIGSe solar cells and proposed that water-soluble Rb compounds are dissolved during the CBD of the CdS buffer layer, and a thin RISe layer on top is left behind [21].

Furthermore, Na and Rb contents are increased for preNa2Rb6. Here, the predeposited Na incorporates itself much better throughout the absorber. Through this increased incorporation, Rb can also access the absorber better.

In Figure 1c, the molar concentrations of Rb and Cd are compared. With increasing Rb amount, less Cd could be detected for variations Na2Rb2, Na2Rb4, Na2Rb6, and Na2Rb8. This was already a known effect in the literature, which is now also observed in ultra-thin CIGSe solar cells and hints at the formation of a $RbInSe_2$ (RISe) surface layer [22, 23].

Interestingly, when combining predeposited Na with Rb PDT, the Cd incorporation increases drastically. When Na is predeposited, more Na incorporates into the absorber, which also enables a higher Rb incorporation. At the same time, the Cd incorporation increases strongly, suggesting that a RISe layer is absent or only present in small amounts. The higher alkali metal concentration simultaneously generates additional Cu vacancies at the front interface, further promoting Cd incorporation.

The lower Cd incorporation for the samples with Na-PDT suggests that this treatment has a catalytic effect on the formation of the RISe layer, since it was observed by S. Lee et al. and T. Kodalle that a RISe surface layer atop the CIGSe absorber hinders CdS growth [9, 24].

EQE measurements across different alkali metal variations can be seen in Figure 2a for Mo and in Figure 2b for ITO.

The first noticeable difference is the broader EQE for ITO. Since the substrates are the only difference, the observation may be attributed to the oxygen from ITO reacting with Ga to form GaO_x. This interface reaction is confirmed by TEM measurements, which reveal the GaO_x layer in Figure S1. An EDX line scan underlines the evidence of the GaO_x layer by showing the increase in Ga and O concentration at the ITO/CIGSe interface. This reaction consumes Ga, lowering the bandgap and extending the EQE to longer wavelengths. The n-type GaO_x may also form a reverse pn-junction, impacting carrier collection [25, 26]. Other compounds, such as (Na and Rb)O_x, may form and introduce defects, additionally affecting the EQE. A further reduction in GGI can result from In diffusion out of the ITO into the absorber, with an In-Se phase reported during three-stage co-evaporation [25].

In Figure 2a,b, small amounts of Rb (Na2Rb2 and Na2Rb4) have little effect on the EQE. At higher Rb amounts (Na2Rb6 and Na2Rb8), a bump appears at 400–500 nm, which is attributed to the CdS layer. It is known that parasitic CdS absorption decreases when a thinner CdS layer forms on the absorber [24]. This suggests that RISe has formed on the absorber surface, hindering the CdS buffer layer formation during CBD [22].

With different alkali metal treatments, the interference spectrum in the wavelength range of approximately 500 to 1000 nm changes most pronouncedly with the appearance of a RISe layer and modified CdS intensity. Notably, in Figure 2b, the preNa2Rb6 sample shows a sharp decline in EQE between 800 and 900 nm, which can be attributed to the pre-DT of Na. Oxygen-related effects from the ITO substrate degrade the absorber quality, leading to lower EQE at longer wavelengths; this effect is absent on Mo substrates, as seen in Figure 2a.

Overall, the impact of the alkali treatment on the EQE is more clearly observed on Mo substrates since additional oxygen-related compounds are less impactful. For the Na+Rb PDT, the biggest difference lies in the decreased parasitic absorption by the CdS buffer layer. In contrast, the preNa2Rb6 sample shows increased parasitic absorption in the short-wavelength range, but the absorber quality seems to have improved due to the pre-DT of Na.

The extracted V_{oc}, J_{sc}, *FF*, and efficiency for ITO and Mo back contact can be seen in Figure 3a–d and are illustrated as boxplots. The average is indicated by the square within the box, the interquartile range by the box itself, and the whiskers show the spread of data. Further away from the whiskers, outliers can be seen as thin lines. The boxplot is taken from at least seven cells per variation.

Figure 3a for Mo substrate shows that the Na2Rb0 variation has a higher V_{oc} and J_{sc} than Na2Rb2 and Na2Rb4, which contain

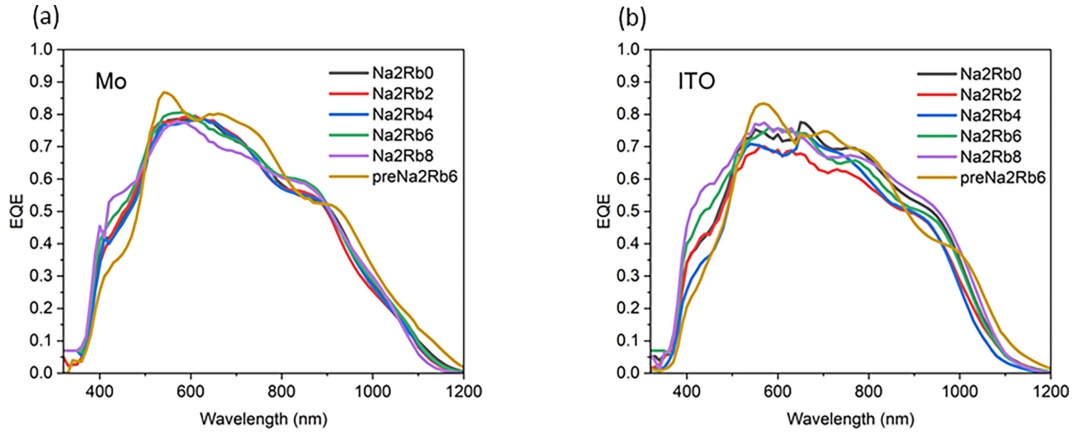

FIGURE 2 | EQE measurement of different alkali metal-treated ultra-thin CIGSe solar cells on (a) Mo back contact and (b) ITO back contact.

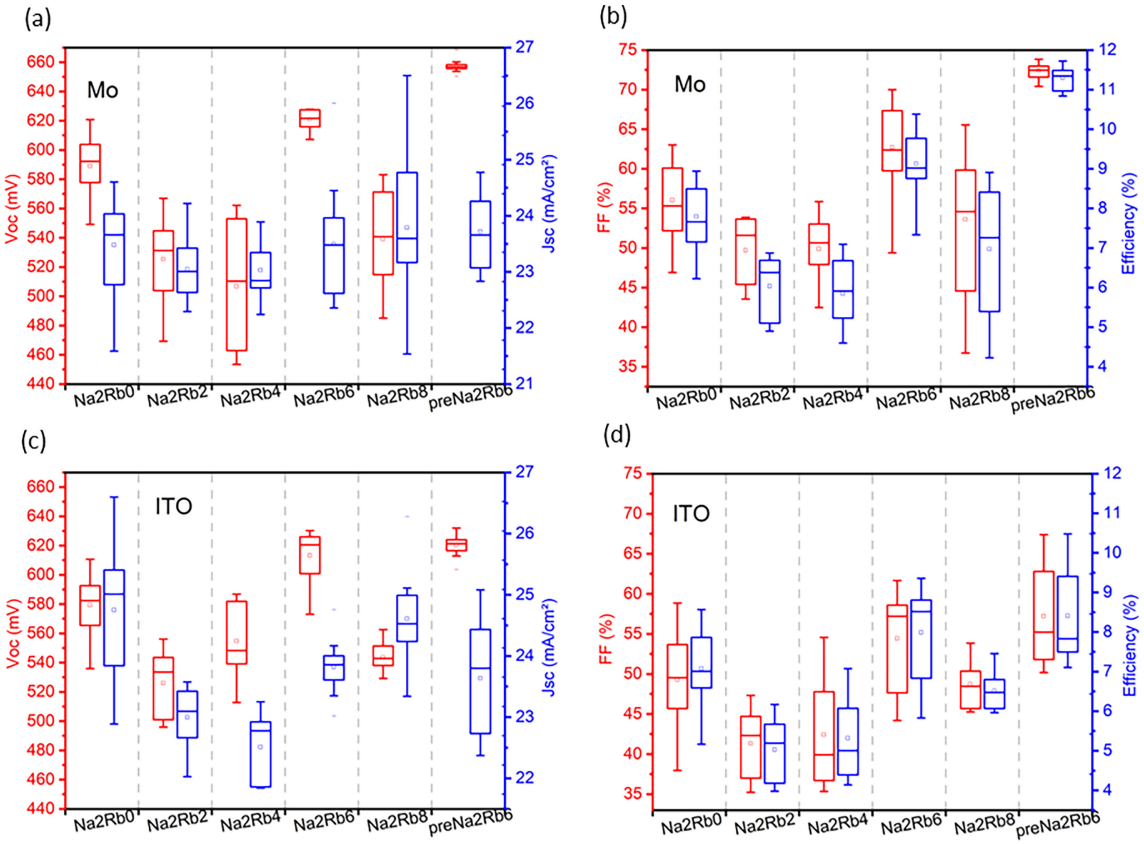

FIGURE 3 | V_{oc}, J_{sc}, *FF*, and efficiency of different alkali metal-treated ultra-thin CIGSe solar cells on (a,b) Mo back contact and (c,d) ITO back contact.

small amounts of Rb. The best performing PDT sample, Na2Rb6, exhibits a significant V_{oc} increase compared to samples with low Rb content, while J_{sc} improves slightly (compare Tables 2 and 3). The Na2Rb8 sample, with the highest Rb content, has a lower V_{oc} than Na2Rb6 but a higher average J_{sc}. Comparing Na2Rb0 and Na2Rb6, V_{oc} improves by 31.84 mV on average, with no significant J_{sc} change due to similar margins of error. The pre-Na2Rb6 sample performs best overall, with the highest V_{oc} of 658.30 mV and a J_{sc} of 24.58 mA/cm^2.

Table 2 and Figure 3 indicate that 6 mg of Rb is the optimal amount for Rb incorporation, with an average *FF* increase of 6.67% when comparing Na2Rb0 with Na2Rb6. When Na is pre-deposited, the average *FF* is further enhanced by 9.65% reaching a maximum of 72.46% for the best cell. In terms of efficiency, an average increase of 1.33% can be seen from Na2Rb0 to Na2Rb6. Efficiencies decrease above or below 6 mg of Rb. Pre-DT of Na further enhances the efficiency on average by 2.14%, with the best cell achieving 11.72%.

According to Figure 3c, the ITO samples follow the V_{oc} trend of the Mo samples, except for preNa2Rb6, which shows a minor V_{oc} increase of 4.81 mV compared to Na2Rb6, whereas for Na2Rb6 compared to Na2Rb0, there was again an average enhancement

TABLE 2 | Electrical data of different alkali metal-treated ultra-thin CIGSe solar cells on Mo substrates.

Variation	V_{oc} (mV)	J_{sc} (mA/cm^2)	*FF* (%)	Efficiency (%)
Na2Rb0	589.01 ± 19.74	23.48 ± 0.74	56.05 ± 4.39	7.79 ± 0.78
	609.66	23.27	63.03	8.94
Na2Rb2	525.31 ± 27.78	23.05 ± 0.53	49.69 ± 4.02	6.04 ± 0.78
	544.73	23.46	53.79	6.87
Na2Rb4	506.76 ± 45.10	23.03 ± 0.53	49.88 ± 4.12	5.85 ± 0.90
	562.16	22.59	55.86	7.10
Na2Rb6	620.85 ± 6.12	23.50 ± 0.94	62.72 ± 5.82	9.12 ± 0.79
	627.89	23.71	70.00	10.38
Na2Rb8	539.11 ± 31.37	23.79 ± 1.35	53.61 ± 9.11	6.97 ± 1.68
	583.17	23.33	65.49	8.91
preNa2Rb6	657.98 ± 5.17	23.66 ± 0.64	72.37 ± 1.09	11.26 ± 0.29
	658.30	24.58	72.46	11.72

Note: Values are averaged over at least seven devices. V_{oc}, J_{sc}, *FF*, and efficiency are shown with (mean ± standard deviation) and the values for the best device.

TABLE 3 | Electrical data of different alkali metal-treated ultra-thin CIGSe solar cells on ITO substrates.

Variation	V_{oc} (mV)	J_{sc} (mA/cm^2)	*FF* (%)	Efficiency (%)
Na2Rb0	579.21 ± 19.89	24.88 ± 1.03	48.95 ± 6.34	7.09 ± 1.11
	610.62	23.84	58.85	8.56
Na2Rb2	525.99 ± 23.59	23.00 ± 0.52	41.32 ± 4.47	5.03 ± 0.84
	556.08	23.43	47.33	6.17
Na2Rb4	554.68 ± 25.81	22.51 ± 0.57	42.42 ± 6.74	5.32 ± 1.02
	586.83	22.10	54.57	7.08
Na2Rb6	613.31 ± 18.37	23.82 ± 0.45	54.44 ± 6.10	7.99 ± 1.18
	625.96	24.10	60.39	9.36
Na2Rb8	543.81 ± 10.20	24.61 ± 0.78	48.72 ± 3.36	6.52 ± 0.48
	562.53	24.62	53.83	7.45
preNa2Rb6	618.12 ± 8.97	23.99 ± 1.18	55.98 ± 6.49	8.31 ± 1.12
	620.00	25.08	67.40	10.48

Note: Values are averaged over at least seven devices. V_{oc}, J_{sc}, *FF*, and efficiency are shown with (mean ± standard deviation) and the values for the best device.

of above 30 mV. J_{sc} decreases for Na2Rb2 and Na2Rb4 compared to Na2Rb0 but recovers at Na2Rb6. Table 3 shows a 0.90% efficiency improvement from Na2Rb0 to Na2Rb6 on ITO, with pre-DT of Na adding another 0.32% gain, thus resulting in 10.48% for the best cell.

Rb enhances electrical performance at controlled amounts on both Mo and ITO substrates. Pre-DT of Na outperforms PDT, and no delamination in combination with Rb is observed. The best PDT sample, Na2Rb6, achieves efficiencies of 10.38% on Mo and 9.36% on ITO. Combining Na pre-DT and Rb PDT yields 11.72% on Mo and 10.48% on ITO. Variations in V_{oc}, J_{sc}, *FF* and efficiency for the different alkali amounts on Mo and ITO are summarized in Tables 2 and 3, respectively.

IVT measurements reveal interface effects impacting CIGSe solar cell performance. Figure 4 presents IVT measurements for CIGSe solar cells on Mo substrates, showing shunt resistance (R_{sh}) variations across different Rb and Na compositions. Figure 5 extends this analysis to ITO substrates, highlighting differences in IV curve behavior and recombination mechanisms due to the transparent back contact.

Na2Rb0 in Figures 4a and 5a are the reference samples to which all other variations are compared. Na2Rb6 and preNa2Rb6 exhibit high R_{sh}, both on Mo and ITO (see Figures 4 and 5d,f). IVT measurements for Na2Rb2, Na2Rb4, and Na2Rb8 display a fan-shaped IV curve pattern, which is more pronounced on ITO (Figure 5b,c,e) than on Mo substrates (Figure 4b,c,e). GDOES

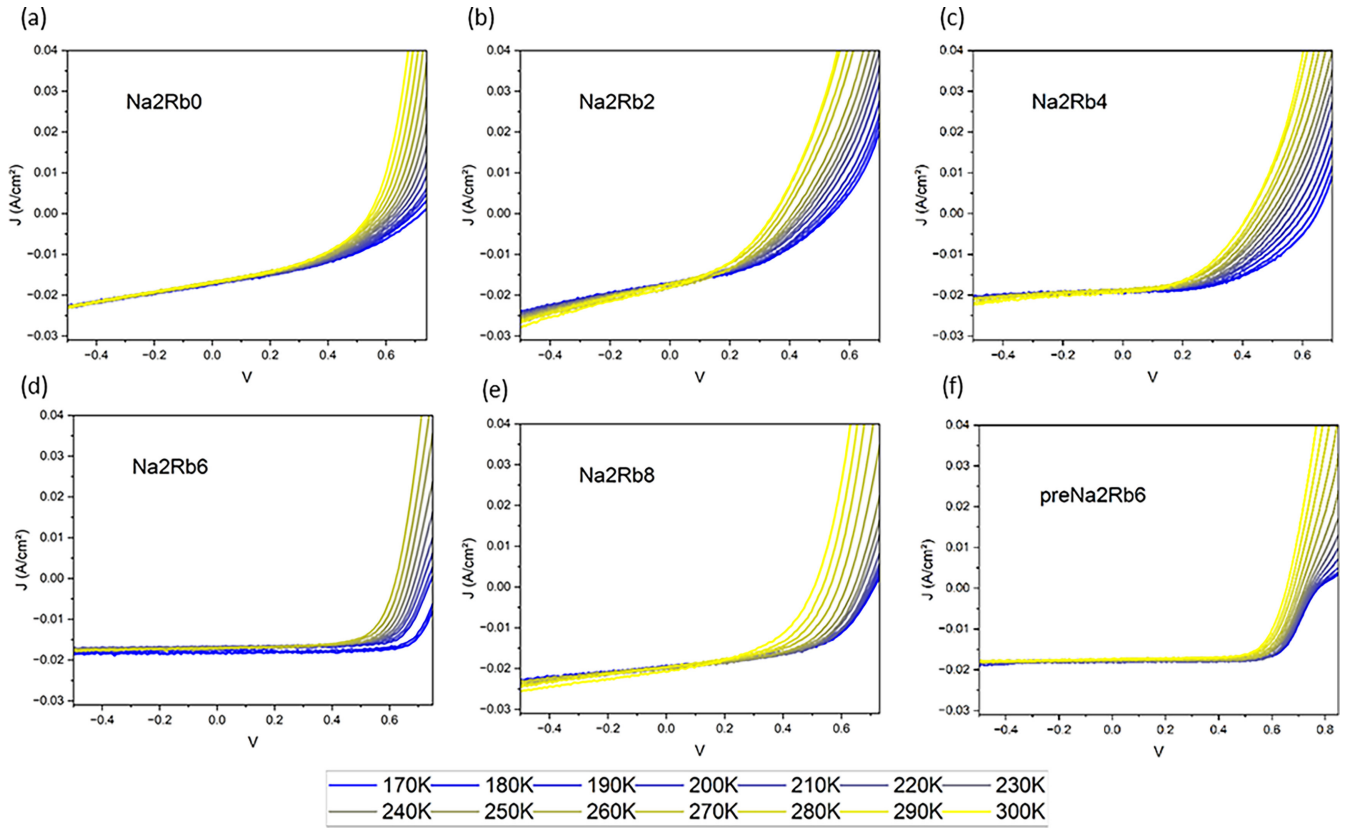

FIGURE 4 | Temperature-dependent IV measurement from 170 K to 300 K of ultra-thin CIGSe solar cells on Mo back contact treated with (a) 2 mg Na, 0 mg Rb; (b) 2 mg Na, 2 mg Rb; (c) 2 mg Na, 4 mg Rb, (d) 2 mg Na, 6 mg Rb; (e) 2 mg Na, 8 mg Rb and (f) 2 mg Na-pre-DT, 6 mg Rb-PDT.

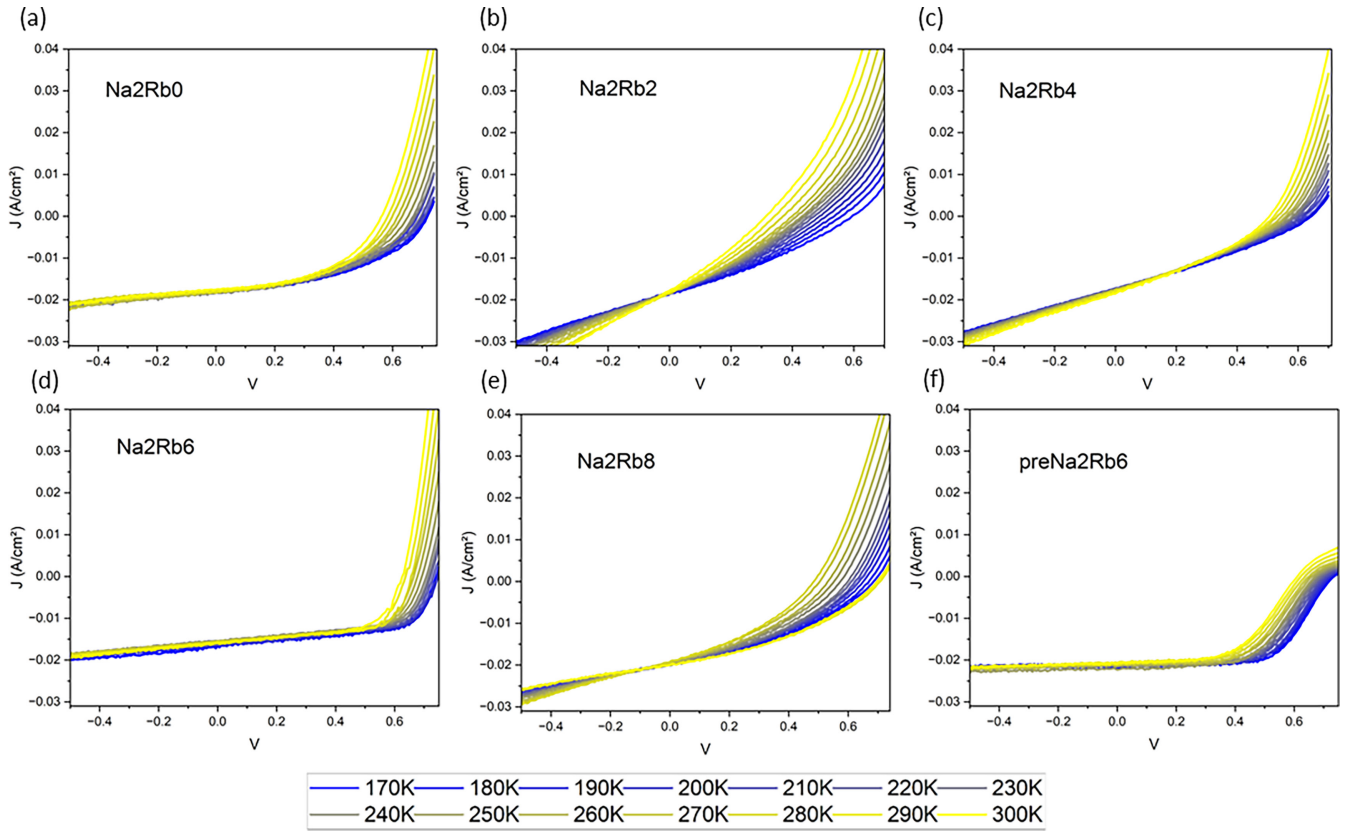

FIGURE 5 | Temperature-dependent IV measurement from 170 K to 300 K of ultra-thin CIGSe solar cells on ITO back contact from treated with (a) 2 mg of Na, 0 mg of Rb; (b) 2 mg of Na, 2 mg of Rb; (c) 2 mg of Na, 4 mg of Rb; (d) 2 mg of Na, 6 mg of Rb; (e) 2 mg of Na, 8 mg of Rb; and (f) 2 mg of Na-pre-DT, 6 mg of Rb-PDT.

measurements (Figure 1b) show that Na2Rb6 and preNa2Rb6 have the highest Rb content in the absorber. Insufficient Rb incorporation (Na2Rb2 and Na2Rb4) reduces the intended passivation effect of alkali metals by pushing out present Na from the absorber while not fully replacing it. Meanwhile, an excess of Rb (Na2Rb8) deteriorates the electrical properties of the absorber, emphasizing that Rb is only beneficial at a certain amount optimized for the respective absorber thickness.

A roll-over effect can be seen for the samples preNa2Rb6, both on Mo and ITO. The origin of the roll-over-effect for Na2Rb6 on ITO (Figure 4f) can be attributed to Na-driven GaO_x formation at the rear interface, visible in Figure S1. GaO_x at the rear-interface is known to cause a Schottky barrier and, because of its high n-type nature, is likely to create a reverse pn-junction [22, 27]. The current blocking behavior of preNa2Rb6 on Mo, on the other hand, will be further analyzed when discussing the IVT measurements in Section 3.2.

By analyzing IV curves at various temperatures, the activation energy (E_a) can be extracted from V_{oc} extrapolated to 0 K. The V_{oc} fitting is performed in the temperature range from 190 to 300 K, as can be seen in Figure S2. Table 4 summarizes the E_a values as extracted from Figure S2a,b, giving further insight into the origins of recombination. The bandgap of the absorbers, extracted from EQE measurements via Tauc plots, ranges from 1.14 to 1.24 eV. Introducing only Na results in an activation energy (E_a) of 0.93 eV for Mo and 1.04 eV for ITO, which serves as a good baseline for comparing the effects of Rb addition.

The decreased E_a for Na2Rb2 on Mo substrate indicates increased interface recombination. For the sample Na2Rb4, E_a has recovered to the same level as Na2Rb0. With further addition of Rb, the E_a increases (Na2Rb6 and Na2Rb8), implying a well-passivated interface. Predepositing Na (preNa2Rb6) decreases E_a compared to Na2Rb6 because of increased alkali metal concentration at the front and rear interface, as visible from Figure 1b.

For ITO substrates, Na2Rb2 and Na2Rb4 exhibit decreased E_a, indicating increased interface recombination. For Na2Rb6, E_a returns to a level comparable to Na2Rb0. Further Rb addition increases E_a for Na2Rb8, suggesting effective interface passivation. Predepositing Na for preNa2Rb6 has a similar E_a to Na2Rb6.

The back barrier, calculated as E_g—E_a, provides further insight into the interface effects (Table 4). At low amounts of Rb (Na2Rb2 and Na2Rb4), the back barrier height increases, indicating increased interface recombination. At higher Rb amounts (Na2Rb6 and preNa2Rb6), the barrier height decreases for Mo, while it increases slightly for ITO as compared to the reference without Rb. The contrasting trends allow the recombination pathways to be pinpointed: Since ITO exhibits increased interface recombination with higher Rb contents, the reduction observed for Mo can be attributed to improved passivation at the CdS/CIGSe interface. In the case of ITO, the increased barrier height indicates that the CIGSe/ITO rear interface contributes additional recombination, likely due to the catalytic interaction of accumulated alkali metals leading to oxygen-related compounds such as GaO_x, which can be seen in the roll-over effect in Figure 5 (f).

The light IVC gives insight into the shunting behavior of the solar cells to identify the best variation of alkali treatment. In Figure 6, the V_{oc} is plotted over the respective light intensity and fitted with the following equation by numerically solving for k_1 and k_2:

$$V_{oc}(G_{avg}) = \frac{2kT}{q} * \ln\left(k_1 * \left(\sqrt{1 + G_{avg} * k_2} - 1\right)\right)$$

The derivation of this equation is extracted through the work of S. Grover et al. and J. Li et al. [28, 29]. It is evident to see that for the respective variations, each measured V_{oc} fits differently to the logarithmic function. The largest deviation is observed for variations Na2Rb2 and Na2Rb4. At low light intensities, both data sets show a steep fall-off in V_{oc}, not allowing a fit to the logarithmic function. Such a behavior has been observed for ultra-thin CIGSe solar cells before and was explained by a low shunt resistance R_{sh} [30].

For Na2Rb0, Na2Rb6, and preNa2Rb6 on Mo, V_{oc} follows a logarithmic dependence, indicating optimal performance. On ITO, only preNa2Rb6 allows a logarithmic V_{oc} fit (Figure 6 (f)).

TABLE 4 | Activation energy E_a extracted from IVT measurement in comparison to the E_g values derived from Tauc plots of the EQE.

	Na2Rb0	Na2Rb2	Na2Rb4	Na2Rb6	Na2Rb8	preNa2Rb6
Activation energy E_a (eV)						
Mo	0.93	0.82	0.92	1.14	1.28	1.02
ITO	1.04	0.78	0.85	0.99	1.17	0.98
Band gap E_g (eV)						
Mo (EQE)	1.22	1.25	1.22	1.24	1.23	1.19
ITO (EQE)	1.18	1.19	1.20	1.18	1.16	1.14
Barrier (eV)						
Mo	0.29	0.43	0.30	0.10	−0.05	0.17
ITO	0.14	0.41	0.35	0.19	−0.01	0.16

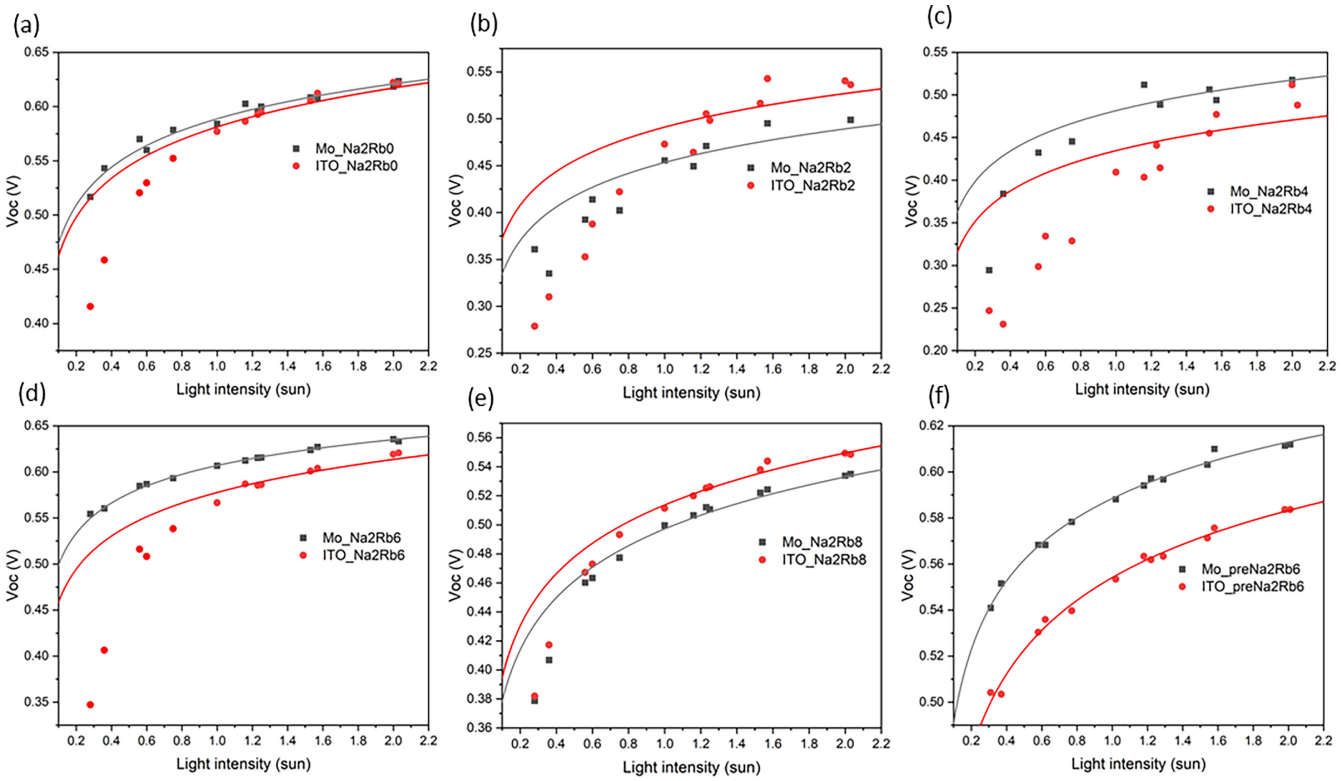

FIGURE 6 | Light intensity-dependent IV measurement from 0.2 to 2.1 suns performed on ultra-thin CIGSe solar cells on Mo and ITO with (a) 2 mg of Na, 0 mg of Rb; (b) 2 mg of Na, 2 mg of Rb; (c) 2 mg of Na, 4 mg of Rb; (d) 2 mg of Na, 6 mg of Rb; (e) 2 mg of Na, 8 mg of Rb; and (f) 2 mg Na-pre-DT, 6 mg Rb-PDT.

Increased recombination at the ITO/CIGSe interface, likely due to GaO_x formation, reduces R_{sh} compared to the respective Mo sample. Yet, the enhanced grain morphology and grain boundary passivation of preNa2Rb6 may compensate for this, yielding higher V_{oc} at low temperatures and enabling the logarithmic dependence.

3.2 | Rb Treatment Combined With Tuning the Ga Gradient

PreNa2Rb6 gave the best performance in the first experiments and thus served as a starting point to investigate the impact of Ga grading, previously shown to enhance performance [26]. For this, during the first stage, a thin In layer is deposited first, followed by Ga and an adjusted amount of In (InGaIn) to maintain comparable GGI. The standard GaIn grading of preNa2Rb6 serves for comparison and was repeated for timely comparison. Furthermore, a GaIn sample with Rb-only treatment was analyzed to assess the influence of Na on the absorber and facilitate the evaluation of interface and bulk effects.

Notably, due to a necessary change in the experimental setup between batches, a vacuum break became necessary between pre-DT of Na and CIGSe absorber deposition for the grading series. To ensure reliable comparison and to account for the possibly increased introduction of oxygen, the preNa2Rb6 baseline is repeated and is named preNa2Rb6_GaIn. This approach allows us to separate the influence of Ga-grading from any artifacts introduced by the process change. Furthermore, to mitigate unwanted GaO_x formation, a different grading is introduced. In this "InGaIn" grading profile, the total In evaporation time is aimed to remain the same as for the standard GaIn sample. However, the sequence is segmented so that one quarter of the In is evaporated before the Ga, followed by the remaining three quarters. This aims to lessen the amount of Ga at the ITO/CIGSe interface, while a sufficient Ga-grading is maintained. XRF data (Table 5) show similar compositions for the different samples. Only preNa2Rb6 with an InGaIn grading has a slightly lower GGI. In this case, the effects of the GGI difference are considered minor compared to the grading effects.

Figure 7 shows the GDOES profiles of the investigated samples. The GGI profiles confirm that Na slows down Ga/In interdiffusion, sharpening the gradient in preNa2Rb6_GaIn, while the Rb6_GaIn sequence produces a flatter profile. Furthermore, an ordered vacancy compound (OVC) layer at the absorber surface may be deduced from the reduction of CGI for Na-treated samples (Figure 7a). The formation of OVCs is confirmed by Raman measurements, as can been seen in Figure S3. D. Schmid et al. showed that Cu deficiencies promote OVC formation, potentially leading to a buried pn-junction [31], and more recently, S. Ishizuka et al. emphasized that effective Rb treatment requires a pronounced "Cu-deficient layer" [32].

During the CBD of CdS, Na and Rb are partly removed, and the remaining Rb residue indicates the previously mentioned thin layer of RISe (Figure 7b measured on the absorber before applying the ZnO layers). These findings are consistent with earlier reports. T. Kodalle described the Cu-poor surface after RbF

TABLE 5 | X-ray fluorescence (XRF) data of CIGSe solar cells with different alkali treatments and grading.

Sample	Absorber thickness	CGI	GGI
preNa2Rb6_GaIn	498.5 ± 3.50	0.88 ± 0.01	0.29 ± 0.01
preNa2Rb6_InGaIn	491 ± 4.00	0.875 ± 0.005	0.265 ± 0.05
Rb6	474.33 ± 4.19	0.883 ± 0.017	0.293 ± 0.009

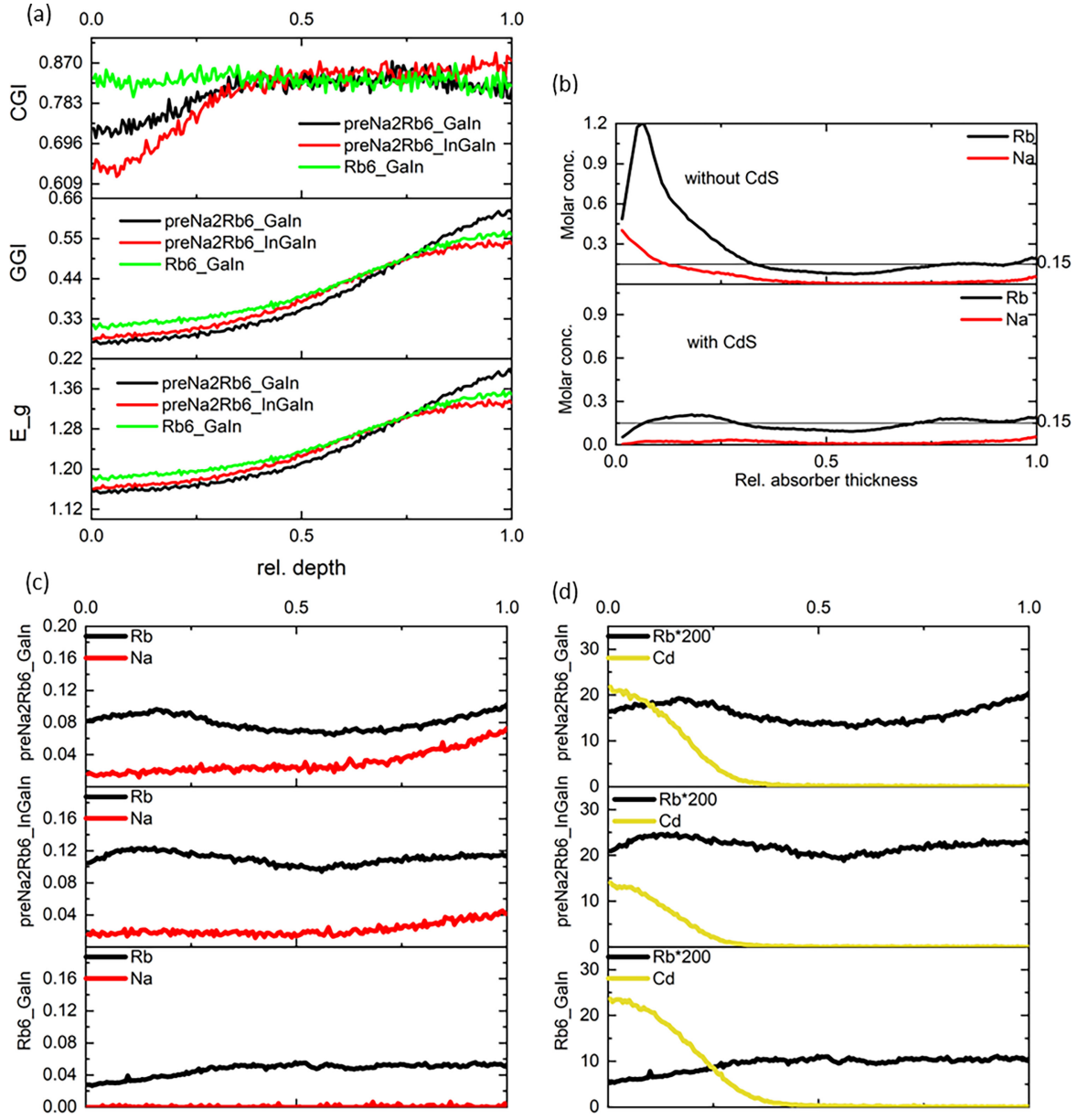

FIGURE 7 | (a) CGI, GGI and bandgap E_g deduced by GDOES. (b) Comparison of Na and Rb concentration before and after CBD of CdS on sample preNa2Rb6_InGaIn (without ZnO layers); (c) Depth-dependent molar concentrations of Na and Rb, and (d) Rb and Cd; for ultra-thin CIGSe solar cells with alkali-metal treatment and Ga-grading variation.

treatment as a "redistribution of Cu" caused by Cu-Rb interdiffusion [9].

Figure 7c emphasizes the importance of the Na treatment for successful Rb incorporation: The Na-treated samples show more than double the Rb concentration than the Rb6_GaIn without Na-treatment.

The Cd incorporation, as observed from Figure 7d, can be explained by the dual role of Rb in the OVC layer: On the one hand, Rb at the surface hinders Cd incorporation through the RISe layer. On the other hand, Rb enhances Cu depletion in the OVC layer through the exchange mechanism between Na and Rb. The increased amounts of Na and Rb in Figure 7b, before the application of CdS, show a high alkali metal activity where

Na can be pushed into the grain interior, forming Na_{Cu}. When Na diffuses out of the grain interior during the cooldown of the absorber, V_{Cu} are left behind, possibly creating OVC compounds (such as $CuIn_3Se_5$ and $CuIn_5Se_8$). These V_{Cu} can then be occupied by Cd as Cd_{Cu}, fostering the CdS growth on top of the absorber.

Our understanding is that the OVC layer forms first, with Na being the primary driver that increases the amount of V_{Cu}, and the additional subsequent Rb treatment is what modifies this OVC layer by further increasing the amount of V_{Cu} and by forming a secondary RISe phase on top of it.

Rb at the surface hinders Cd incorporation, but Rb simultaneously enhances Cu depletion in the OVC layer, providing additional V_{Cu} that can be occupied by Cd as Cd_{Cu}, possibly promoting the CdS growth on top of the absorber. preNa2Rb6_InGaIn exceeds a threshold where sufficient Rb remains in the OVC layer to suppress Cd growth, indicating a RISe surface layer.

The nongraded preNa2Rb6_GaIn and Rb6_GaIn, in comparison, show high Cd incorporation with reduced amounts of Rb. Na predeposition facilitates Rb incorporation into the absorber, reducing RISe formation and supporting Cd incorporation by leaving behind an OVC layer. Both the n-type RISe [14], and n-type Cd_{Cu} [24] can form at the surface and contribute to a buried pn-junction, changing the band alignment.

From these considerations, it can be deduced that the OVC has two functions. Firstly, it adjusts the band alignment on the surface with its V_{Cu}-rich compounds on the absorber surface, making it Cu-deficient. Secondly, the OVC layer acts as the growth foundation for the subsequent RISe and Cd_{Cu}/CdS surface phases.

The OVC layer impact scales with alkali metal incorporation, with preNa2Rb6_InGaIn showing the most Cu-deficient OVC layer. Since the differences in alkali metal and Cd incorporation are large between preNa2Rb6_GaIn and preNa2Rb6_InGaIn, it remains difficult to assess whether the gradient itself has a significant influence beyond its impact on the varying alkali metal incorporation.

Figure 8 presents the EQE spectra for the ultra-thin CIGSe solar cells with different alkali-metal treatment and Ga-grading variation on Mo and ITO substrates. For Mo (Figure 8a) preNa2Rb6_InGaIn shows reduced parasitic absorption around 430–450 nm, which can be directly correlated to a thinner CdS layer; see Figure 7d. This results in a clear EQE increase in the short-wavelength region compared to the other variations.

For ITO (Figure 8b) no significant change in CdS-related absorption is observed, suggesting a similar CdS thickness across all variations (*note:* GDOES measurements were performed on samples with Mo substrates only). Beyond 520-nm wavelength, preNa2Rb6_GaIn exhibits the highest EQE, followed by preNa2Rb6_InGaIn.

The difference in CdS-related absorption between Mo and ITO substrates may be attributed to the Na pre-DT application and the substrates' control over Na incorporation. Mo substrates have a Na-barrier that blocks Na diffusion into the absorber and vice versa (Figure S4), whereas ITO is sputtered onto Na-poor glass, not providing Na and also not restricting its indiffusion. In this sample series, Na was predeposited with a vacuum break, allowing sufficient time for Na to diffuse through the ITO layer into the glass during the preheating for the co-evaporation of the absorber. This can result in reduced Na availability during the formation of the absorber. In contrast, in the first sample series, the absorber was deposited immediately after Na deposition, minimizing Na loss.

On Mo, as shown in Figure 8a, the reduced parasitic absorption reveals the effectiveness of the Na barrier. It also upholds the previous explanation that preNa2Rb6_InGaIn exceeds a threshold where sufficient Rb remains in the OVC layer to suppress Cd growth. In contrast, preNa2Rb6_GaIn has less Na incorporation, which consequently results in a lower amount of Rb, and therefore, the observed increased Cd incorporation.

When comparing the pre-DT Na samples with the sample without Na pre-DT on ITO in Figure 8b, it becomes evident that the presence of Rb at the surface influences the parasitic absorption of the CdS layer in a similar way for all ITO samples. This suggests that the level of Rb incorporation is comparable across the entire ITO series.

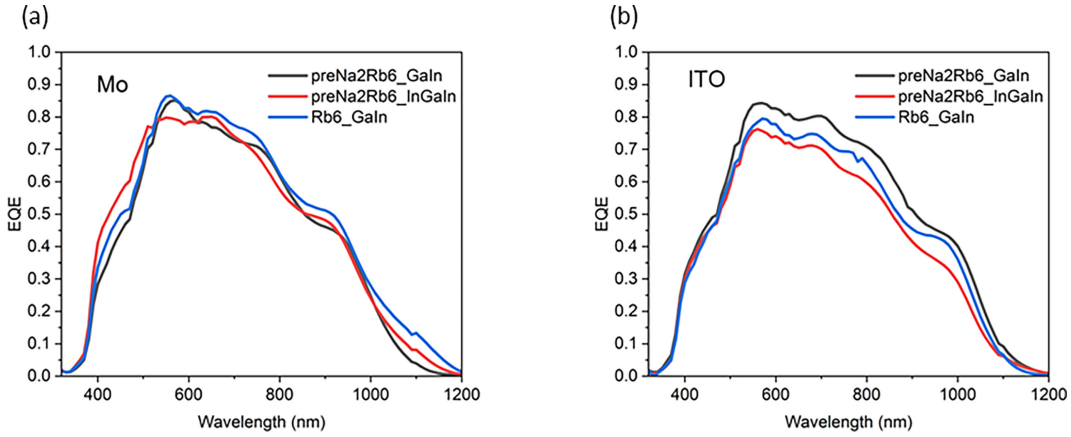

FIGURE 8 | EQE measurement for ultra-thin CIGSe solar cells with different alkali-metal treatment and Ga-grading variation on (a) Mo and (b) ITO.

The IV results, in Figure 9 and Tables 6 and 7, show the highest V_{oc} for preNa2Rb6_InGaIn with 625.45 mV on average on Mo, despite its flatter GGI and E_g profile compared to preNa2Rb6_GaIn. GDOES analysis (Figure 7a) revealed that this sample also has the most Cu-deficient OVC layer. The OVC layer can improve the band alignment at the CIGSe/CdS interface, effectively acting as an additional grading and thereby contributing to the observed V_{oc} increase. Furthermore, the OVC layer also indicates the formation of the RISe layer on top of it, further improving the band alignment.

For Mo substrates in Table 6, both V_{oc} and J_{sc} are lower when Na is absent (V_{oc} = 560.92 mV and J_{sc} = 21.80 mA/cm^2 for Rb6_GaIn vs. V_{oc} = 598.57 mV and J_{sc} = 23.25 mA/cm^2 for preNa2Rb6_GaIn on average). In contrast, the *FF* is by an average of 3.70% lower with Na (preNa2Rb6_GaIn compared to Rb6_GaIn). A similar *FF* loss was reported by Kodalle et al. [11] and attributed to alkali migration towards the transparent front contact, where it activates acceptor states. This argument is supported by Na being detected throughout the entire solar cell (Figure S4a–c). The overall efficiency is still higher for the preNa samples. The comparison between Na predeposition and the absence of Na further emphasizes the beneficial role of Na for solar cells on Mo. By adding Na as a pre-DT, the efficiency increases by 0.56% and by changing the Ga grading, another increase of 0.69% can be achieved.

For the ITO substrates in Table 7, the electrical data show a different trend than on Mo. Rb6_GaIn has a higher average V_{oc} (566.22 mV) than its counterpart preNa2Rb6_GaIn (550.34 mV). However, when combining grading modification with Na pre-DT, the average V_{oc} reaches 596.57 mV. The J_{sc} behaves oppositely, with the highest value for preNa2Rb6_GaIn (23.81 mA/cm^2), followed by Rb6_GaIn (22.70 mA/cm^2) and

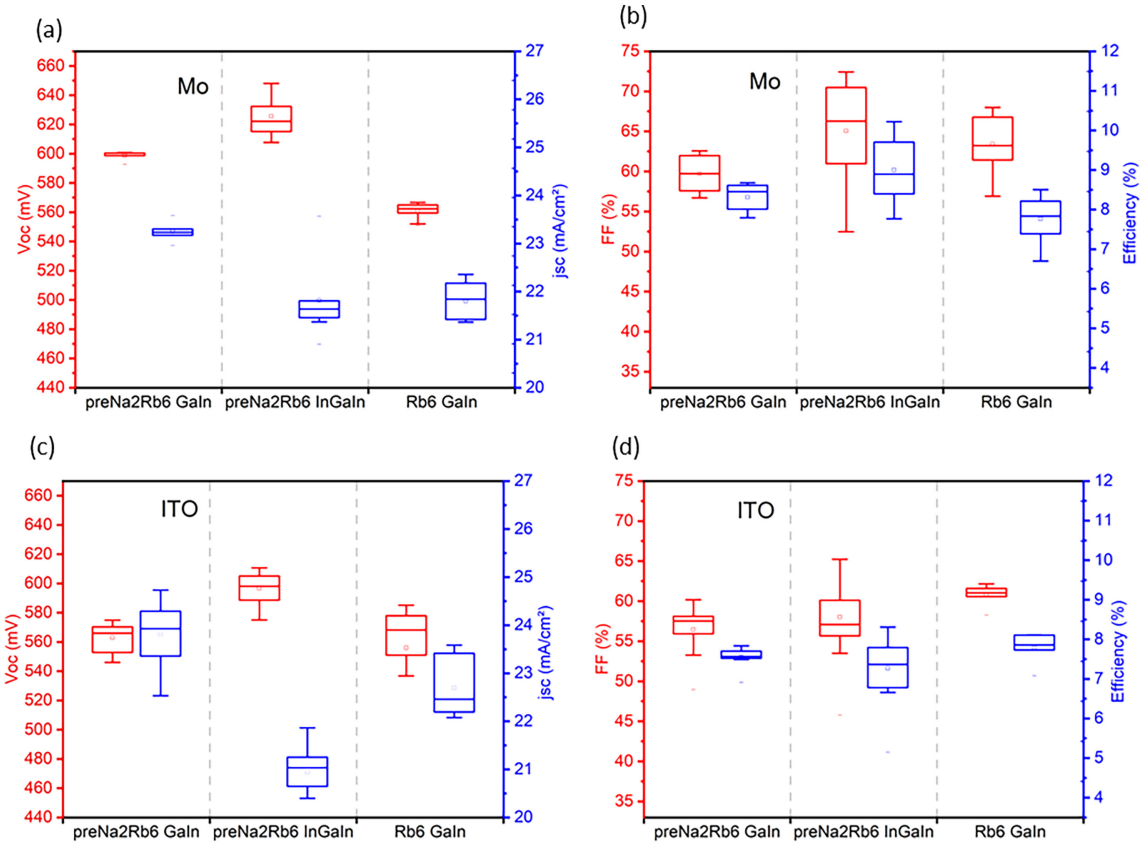

FIGURE 9 | V_{oc}, J_{sc}, *FF*, and efficiency for ultra-thin CIGSe solar cells with different alkali-metal treatment and Ga-grading variation on (a, b) Mo and (c, d) ITO.

TABLE 6 | Electrical data of ultra-thin CIGSe solar cells with different alkali-metal treatment and Ga-grading variation on Mo substrates.

Variation	V_{oc} (mV)	J_{sc} (mA/cm^2)	FF (%)	Efficiency (%)
preNa2Rb6_GaIn	598.57 ± 3.96	23.25 ± 0.23	59.71 ± 2.59	8.31 ± 0.39
	600.85	23.58	62.56	8.68
preNa2Rb6_InGaIn	625.45 ± 12.31	21.82 ± 0.68	65.05 ± 5.95	9.00 ± 0.75
	648.09	23.56	72.42	10.22
Rb6_GaIn	560.92 ± 5.28	21.80 ± 0.36	63.41 ± 3.35	7.75 ± 0.58
	566.73	22.36	67.98	8.51

Note: V_{oc}, J_{sc}, *FF*, and efficiency are shown with (mean ± standard deviation) and the values for the best device.

preNa2Rb6_InGaIn (20.93 mA/cm^2). The average *FF* and efficiency are both lower with Na pre-DT, so that the highest average efficiency of 8.11% is achieved for Rb6_GaIn. Yet, the overall best efficiency measured on ITO was 8.31% for a preNa2Rb6_InGaIn sample, highlighting the potential of grading modification.

In the first sample batch, the Na pre-DT had a less positive impact on the overall efficiency for ITO compared to Mo back contact (compare Tables 2 and 3). In the Ga grading batch with Na pre-DT followed by a vacuum break, the average electrical performance decreases for both Mo and ITO, hinting at equal introduction of defects at the (Mo/ITO)/CIGSe interface or worse absorber quality. As a conclusion, controlling oxygen diffusion between the back contact and the absorber appears to be even more critical in the presence of Na.

Figure 10 summarizes the IVT results for the investigated samples on Mo and ITO. The results for both substrates are very similar. The main difference lies in R_{sh}, which is lower on ITO and likely relates to increased interface recombination at the ITO/CIGSe interface compared to Mo/CIGSe [33–35].

In Figure 10a,c,d,f Na-treated and non–Na-treated samples can be directly compared. Here, the addition of Na in combination with Rb increases R_{sh}, indicating that Na passivates recombination pathways.

A current-blocking behavior can be observed at low temperatures for the same samples. It can be ruled out that GaO_x is the only cause, since the roll-over effect cannot be observed at room temperature, as in Figure 5f, and moreover, it is not exclusive to the ITO substrate.

TABLE 7 | Electrical data of ultra-thin CIGSe solar cells with different alkali-metal treatment and Ga-grading variation on ITO substrates.

Variation	V_{oc} (mV)	J_{sc} (mA/cm^2)	FF (%)	Efficiency (%)
preNa2Rb6_GaIn	550.34 ± 3.27	23.81 ± 0.67	56.45 ± 3.24	7.55 ± 0.25
	552.91	24.73	60.17	7.83
preNa2Rb6_InGaIn	596.57 ± 10.87	20.93 ± 0.57	58.02 ± 5.28	7.26 ± 0.85
	610.62	21.86	65.22	8.31
Rb6_GaIn	566.22 ± 15.16	22.70 ± 0.65	60.77 ± 1.35	7.79 ± 0.38
	585.11	23.59	62.17	8.11

Note: V_{oc}, J_{sc}, *FF*, and efficiency are shown with (mean ± standard deviation) and the values for the best device.

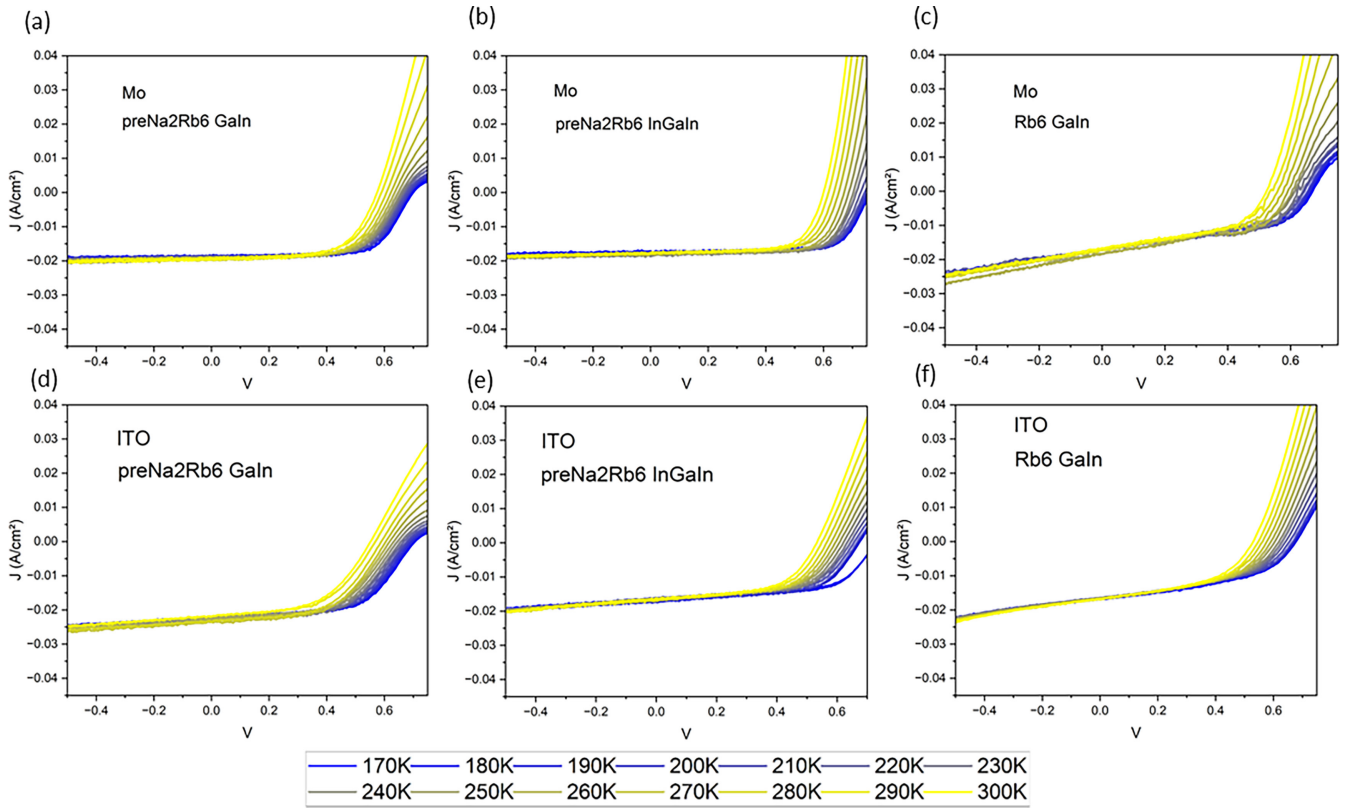

FIGURE 10 | Temperature-dependent IV measurement from 170 to 300 K of solar cells on Mo with (a) 2 mg of pre-DT-Na, 6 mg of Rb; (b) 2 mg of pre-DT-Na, 6 mg of Rb and adjusted Ga gradient; (c) 0 mg of Na, 6 mg of Rb, and on ITO with (d) 2 mg of pre-DT-Na, 6 mg of Rb; (e) 2 mg of pre-DT-Na, 6 mg of Rb, and adjusted Ga gradient; and (f) 0 mg of Na, 6 mg of Rb.

Several mechanisms must be considered for the current-blocking behavior:

1. Na deficiency can produce a current-blocking barrier at the CIGSe/(Mo/ITO) interface [22, 36]
2. An excess of Na can introduce deep defects in the CIGSe absorber [30, 37, 38]
3. Increased thickness of CdS and band offset through the OVC layer create a current blocking behavior at the CIGSe/CdS interface [32, 39]

In Figure 10c, the roll-over observed for Rb6_GaIn originates from the absence of Na. Insufficient Na content in CIGSe absorbers has been shown to correlate with low doping density and a high back barrier height E_h compared to Na-treated absorbers. At lower temperatures, the effective charge carrier density decreases further along with a rising E_h, leading to the temperature-dependent roll-over effect [36].

For preNa2Rb6_GaIn and preNa2Rb6_InGaIn, the front and back interface must be considered since Cd, Na, and Rb concentrations vary.

In Figure 7c, preNa2Rb6_GaIn shows double the amount of Na concentration at the CIGSe/(Mo/ITO) back interface than preNa2Rb6_InGaIn.This can be the origin of the roll-over effect since an excess Na content is known to increase the deep defect formation and net doping density [37]. S. Puttnins et al. expected that a "tunnelling enhanced interface recombination" is likely due to too high charge carrier density [37].

From Figure 7, we concluded that at the front interface for preNa2Rb6_GaIn, no uniform RISe layer forms, and for preNa2Rb6_InGaIn, a RISe layer likely exists. The nonuniform RISe layer was accompanied by an increased amount of Cd, indicating a thicker CdS layer. Ishizuka et al. showed that OVC layer compounds like $CuIn_3Se_5$ have a lower conduction band minimum than $CuInSe_2$, see Table 8 [39]. Thus, the spike-like transition from $CuIn_3Se_5$ to CdS would be higher.

The combination of a thicker CdS layer and a steeper CBM spike at the CIGSe/CdS layer can lead to a more pronounced current blocking barrier. In contrast, if RISe forms on top of the OVC layer, the band gap difference of the conduction band minimum is right in between $CuIn_3Se_5$ and CdS. RISe has the further effect of lowering the CdS thickness, which reduces the total parasitic absorption.

The activation energies E_a, extracted from the IVT measurements and given in Table 9, support this interpretation: Bulk recombination dominates only in preNa2Rb6_InGaIn on Mo, where the Cd incorporation is lowest and the Na concentration at the back interface is at a moderate amount. Vice versa, for the preNa2Rb6_GaIn sample on Mo, the lower E_a is related to the thicker Cd layer at the front and a high Na content at the rear interface. Rb6_GaIn has the lowest activation energy owing to the missing Na passivation of the CIGSe/Mo interface and grain boundaries.The E_a for the ITO samples with Na pre-DT shows similar activation energies except for preNa2Rb6_InGaIn, where surprisingly the CIGSe/Mo interface benefits most from the InGaIn grading. The Na-free Rb6_GaIn sample, with its higher barrier height, shows that no Na-treatment also increases the interface recombination.

As Cd and alkali metal incorporation vary significantly between graded and nongraded samples, it can be concluded that alkali metal incorporation is modified by grading and that the alkali metal amount has to be adjusted according to the different alkali metal incorporation.

TABLE 8 | Conduction band minima (CBM) and valence band maxima (VBM) for compounds present at the CIGSe/CdS interface, the values for $RbInSe_2$.

	Conduction band minimum (eV)	Valence band maximum (eV)
$CuInSe_2$	−4.26 [39]	−5.25 [39]
$CuIn_3Se_5$	−4.48 [39]	−5.65 [39]
$CuIn_5Se_8$	−4.5 [40]	−5.75 [40]
$RbInSe_2$	−4.225 [9]	−7.005 [9]
CdS	−3.95 [40]	−6.37 [39]

TABLE 9 | Activation energy E_a extracted from IVT measurement in comparison to the E_g derived from Tauc plots of the EQE.

	preNa2Rb6_GaIn	preNa2Rb6_InGaIn	Rb6_GaIn
Activation energy E_a (eV)			
Mo	1.04	1.13	0.98
ITO	1.04	1.05	0.98
Bandgap E_g (eV)			
Mo (EQE)	1.20	1.22	1.21
ITO (EQE)	1.15	1.17	1.17
Barrier height (eV)			
Mo	0.16	0.08	0.23
ITO	0.11	0.12	0.19

3.3 | Discussion

To visualize the structural formation during absorber growth, the mechanistic model in Figure 11 illustrates the interplay between Na, Rb, OVC, and Cd. Na pre-DT and Na PDT influence how the Na incorporates and distributes itself in the absorber. This difference in Na incorporation is directly correlated to Rb incorporation, since Rb pushes the Na away to take its place. Moreover, Rb incorporation is correlated with the OVC layer formation at the surface of the absorber, where a RISe layer grows depending on the amount of Rb incorporated, which is further dependent on the Na pre-DT or PDT. GDOES data in Figures 1 and 7 suggest that CdS growth is facilitated by the OVC layer and hindered by the RISe layer.

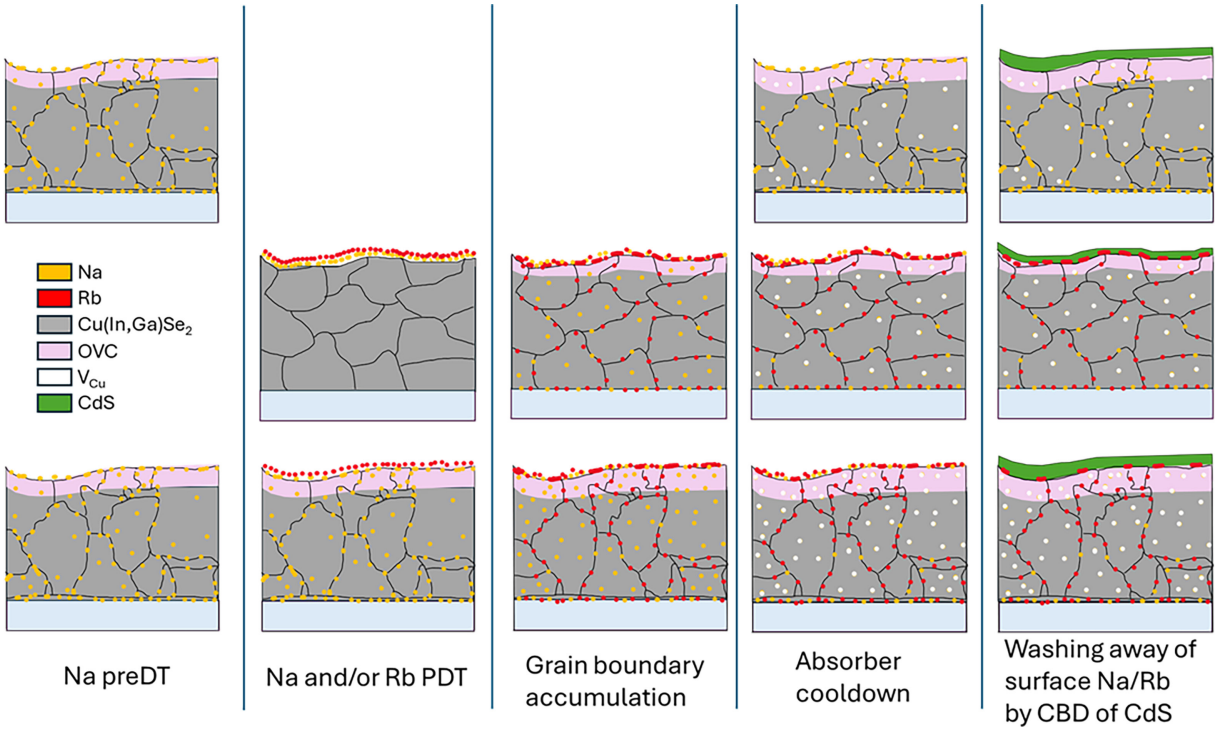

FIGURE 11 | Mechanistic model for the Na–Rb exchange mechanism and the OVC + RISe formation for samples with only Na pre-DT in the top row, Na + Rb PDT in the middle row and Na pre-DT+Rb PDT in the bottom row.

To gain a better understanding of these closely interwoven relations, the mechanistic model in Figure 11 was developed.

In the top row, the Na accumulation at the grain boundaries, grain interior, and interfaces is shown for Na pre-DT. When Na accumulates at the grain interior, it occupies copper vacancies (V_{Cu}). This occurs especially in the third stage, as the absorber transitions from Cu-rich to Cu-poor stoichiometry, resulting in a higher density of V_{Cu} towards the absorber surface.

OVCs originate from intrinsic Cu-deficiency, which is facilitated by the Na occupying Cu-sites. As the absorber cools down, Na diffuses out of the grain interior, leaving behind V_{Cu}. The visible OVC layer in the top row is a result of Cu-poor stoichiometry and Na accumulation towards the surface. Any residual Na at the surface is then washed away during the CBD, only leaving behind the CdS layer.

In the middle row, the Na+Rb PDT is shown. After absorber growth, Na is deposited first and incorporates itself into the grain boundaries; however, for the same amount of evaporated Na, compared to Na pre-DT, less Na is incorporated into the bulk of the absorber and more Na remains at the absorber surface.

Afterwards, Rb is deposited, pushing the Na away from the grain boundary and into the grain interior via the Na–Rb exchange mechanism [6]. Rb boosts the V_{Cu} occupation density by Na, especially in the surface region where most of the Na and Rb accumulate due to PDT. The increase of V_{Cu} occupation density of Na has a catalytic effect on the OVC growth, while simultaneously, the excess Na presence at the surface acts as a chemical precursor that facilitates the formation of a RISe layer [9].

Cooling down the absorber causes the Na to diffuse out of the grain interior, leaving behind V_{Cu}, while residual Na, Rb, and a RISe layer remain on the surface. During CBD of CdS, the Na and Rb are washed away while a thin RISe layer remains, which hinders CdS formation and leads to an overall thinner CdS layer.

The bottom row shows a combination of Na pre-DT and Rb PDT. In this case, Na behaves similarly as in the top row until Rb is deposited after absorber formation.

Compared to Na+Rb PDT, much more Na is incorporated into the absorber for Na pre-DT + Rb PDT, as seen in Figure 1b. This change in Na concentration and distribution has two primary effects: First, increased amounts of Na in the absorber increase the Rb incorporation by boosting the Na–Rb exchange mechanism, forcing more Na into the grain interior. Second, less Na is expected at the surface of the absorber, which is necessary for RISe layer growth, resulting in a less pronounced RISe formation. Consequently, cooling down the absorber results in a thicker OVC layer and a thinner RISe layer.

When depositing CdS onto the absorber, residual Na and Rb at the surface are washed away; however, compared to the Na + Rb PDT, a thinner RISe layer remains. The now exposed OVC acts as a nucleation site that facilitates the growth of a thicker CdS layer.

The mechanistic model in Figure 11 highlights how the combination of multi-alkali treatment affects the surface chemistry of the CIGSe absorber. The Na pre-DT results in a higher bulk Na concentration that serves as a catalyst enhancing Rb incorporation deep inside the absorber and boosting the subsequent NaRb exchange mechanism. Compared to Na PDT, Na pre-DT results in less residual Na at the surface, while overall, more Rb can be incorporated. This suppresses the RISe formation in favor of a pronounced OVC layer at the absorber surface. In contrast, the Na PDT prepares the absorber surface for the growth of a RISe layer while also providing a foundation for OVC layer formation. Finally, observing the transition from a growth-facilitating (OVC layer) to a growth-inhibiting (RISe layer) surface for the CdS formation demonstrates that the sequence of alkali metal incorporation is just as critical as the amount evaporated.

4 | Conclusions

Rb incorporation and carefully optimized alkali treatments can significantly enhance the device performance of ultra-thin CIGSe solar cells. The comprehensive variation of Rb revealed that the best performing configuration was achieved with predeposited Na followed by PDT Rb (preNa2Rb6), yielding an efficiency of 11.72% on Mo and 10.48% on ITO.

The results show that Rb influences not only the absorber but also the CIGSe/CdS interface by modifying Cd incorporation. Overall, an optimized amount of Rb improves device efficiency by firstly enhancing the beneficial role of Na through the Na–Rb exchange mechanism, pushing Na into the grains, and providing itself superior grain boundary passivation.

Secondly, Rb at the absorber front can control the formation of an OVC layer, which increases Cd incorporation, or a uniform RISe layer on top of it, which hinders Cd incorporation. If the RISe layer grows on top of the absorber, the CdS buffer thickness is reduced, thereby lowering parasitic absorption, while maintaining a high V_{oc} of 657.98 mV for Mo through improved band alignment.

It is observed that when Na and Rb are deposited only as PDT, Cd deposition is hindered by the RISe layer, while the combination of predeposited Na and Rb PDT drastically increases Cd incorporation. The decreased Cd incorporation for Na + Rb PDT suggests a catalytic effect of Na on the RISe surface layer growth.

IVT measurements could distinguish between interface- and bulk-related pathways. They also revealed differences between GaO_x-related Schottky barriers at the ITO interface and Rb-related barriers, with the latter becoming visible only at low temperatures. When Rb is introduced without Na, a current-blocking barrier forms due to the absence of Na-related passivation. In contrast, the combined presence of Na and Rb introduces more complex behavior, which can be attributed either to a back-interface barrier caused by deep defects associated with excess Na or to an enhanced CBM spike at the CIGSe/CdS interface or to a combination of both effects. These effects can be mitigated through precise Na and Rb deposition so that the interplay between them can maximize grain boundary and interface passivation while increasing the V_{Cu}, beneficial for charge carrier concentration.

Finally, introducing small amounts of In at the beginning of the absorber process further enhanced performance. The InGaIn deposition sequence on Mo suppressed Rb-related current blocking barriers, increased alkali metal incorporation, and promoted a RISe layer on top of an OVC layer, favorable for smoother band alignment. This highlights the synergistic potential of combining alkali doping with band-gap engineering to push the efficiency of ultra-thin CIGSe solar cells.

Author Contributions

Christoph Rath was responsible for conceptualization, investigation, formal analysis, writing original draft, and finalizing the manuscript. Tristan Köhler was responsible for the deposition of i-ZnO, Al:ZnO, and Al-grids, experimental troubleshooting and supporting the analysis. Martina Schmid was responsible for resources, supervision, formal analysis, review, and editing.

Acknowledgments

The authors thank the Deutsche Forschungsgemeinschaft (DFG) for funding the instrument for the measurement of GDOES and XRF (INST 20876/324-1 FUGG), which is acknowledged as follows: "Gefördert durch die Deutsche Forschungsgemeinschaft (DFG) Projektnummer INST 20876/324-1 FUGG". Further thanks go to Yao Gao for providing insights about IVT and IVC measurements, Ihab Kardosh for providing Raman measurements, and to Jan Berger for discussion. Many thanks go to Markus Heidelmann from the ICAN who made a TEM measurement and provided the EDX line scan. The authors acknowledge support from the Open Access Publication Fund of the University of Duisburg-Essen through the project DEAL. Open Access funding enabled and organized by Projekt DEAL.

Funding

This work was supported by the Deutsche Forschungsgemeinschaft (DFG, INST 20876/324-1 FUGG) and the Open Access Publication Fund of the University of Duisburg-Essen through the project DEAL.

Data Availability Statement

The data that support the findings of this study are available from the corresponding author upon reasonable request.

References

1. D. Kim, S. S. Shin, S. M. Lee, et al., "Flexible and Semi-Transparent Ultra-Thin CIGSe Solar Cells Prepared on Ultra-Thin Glass Substrate: A Key to Flexible Bifacial Photovoltaic Applications," *Advanced Functional Materials* 30, no. 36 (2020): 2001775.

2. J. Hedstrom, H. Ohlsen, M. Bodegard, et al., *ZnO/CdS/Cu (In, Ga) Se/Sub 2/Thin Film Solar Cells With Improved Performance* (IEEE, 1993).

3. J. Keller, K. Kiselman, O. Donzel-Gargand, et al., "High-Concentration Silver Alloying and Steep Back-Contact Gallium Grading Enabling Copper Indium Gallium Selenide Solar Cell With 23.6% Efficiency," *Nature Energy* 9, no. 4 (2024): 467–478.

4. R. Sakdanuphab, C. Chityuttakan, A. Pankiew, N. Somwang, K. Yoodee, and S. Chatraphorn, "Growth Characteristics of Cu (In, Ga) Se2 Thin Films Using 3-Stage Deposition Process With a NaF Precursor," *Journal of Crystal Growth* 319, no. 1 (2011): 44–48.

5. D. Braunger, D. Hariskos, G. Bilger, U. Rau, and H. W. Schock, "Influence of Sodium on the Growth of Polycrystalline Cu (In, Ga) Se2 Thin Films," *Thin Solid Films* 361 (2000): 161–166.

6. M. Krause, S. Moser, C. Mitmit, S. Nishiwaki, A. N. Tiwari, and R. Carron, "Precise Alkali Supply During and After Growth for High-Performance Low Bandgap (Ag, Cu) InSe2 Solar Cells," *Solar RRL* 8, no. 10 (2024): 2400077.

7. S.-H. Wei, S. B. Zhang, and A. Zunger, "Effects of Na on the Electrical and Structural Properties of CuInSe 2," *Journal of Applied Physics* 85, no. 10 (1999): 7214–7218.

8. D. Rudmann, *Effects of Sodium on Growth and Properties of Cu (In, Ga) Se2 Thin Films and Solar Cells* (Verlag nicht ermittelbar, 2004).

9. T. Kodalle, *Unraveling the Structural and Optoelectronic Effects of Rb on Chalcopyrite Solar Cells* (Dissertation, Martin-Luther-Universität Halle-Wittenberg, 2020).

10. C. Zhao, S. Yu, W. Tang, et al., "Advances in CIGS Thin Film Solar Cells With Emphasis on the Alkali Element Post-Deposition Treatment," *Materials Reports: Energy* 3, no. 3 (2023): 100214.

11. T. Kodalle, M. D. Heinemann, D. Greiner, et al., "Elucidating the Mechanism of an RbF Post Deposition Treatment in CIGS Thin Film Solar Cells," *Solar Rapid Research Letters* 2, no. 9 (2018): 1800156.

12. T. P. Weiss, S. Nishiwaki, B. Bissig, et al., "Injection Current Barrier Formation for RbF Postdeposition-Treated Cu (In, Ga) Se2-Based Solar Cells," *Advanced Materials Interfaces* 5, no. 4 (2018): 1701007.

13. N. Taguchi, S. Tanaka, and S. Ishizuka, "Direct Insights Into RbInSe2 Formation at Cu (In, Ga) Se2 Thin Film Surface With RbF Postdeposition Treatment," *Applied Physics Letters* 113, no. 11 (2018): 113903.

14. M. Malitckaya, H.-P. Komsa, V. Havu, and M. J. Puska, "Effect of Alkali Metal Atom Doping on the CuInSe2-Based Solar Cell Absorber," *Journal of Physical Chemistry C* 121, no. 29 (2017): 15516–15528.

15. S. Thomas, T. Bertram, C. Kaufmann, et al., "Effects of Material Properties of Band-Gap-Graded Cu (In, Ga) Se2 Thin Films on the Onset of the Quantum Efficiency Spectra of Corresponding Solar Cells," *Progress in Photovoltaics: Research and Applications* 30, no. 10 (2022): 1238–1246.

16. P. E. Lippens and M. Lannoo, "Calculation of the Band Gap for Small CdS and ZnS Crystallites," *Physical Review B* 39, no. 15 (1989): 10935–10942.

17. M. Saifullah, D. Kim, J.-S. Cho, et al., "The Role of NaF Post-Deposition Treatment on the Photovoltaic Characteristics of Semi-transparent Ultrathin Cu (In, Ga) Se 2 Solar Cells Prepared on Indium-Tin-Oxide Back Contacts: A Comparative Study," *Journal of Materials Chemistry A* 7, no. 38 (2019): 21843–21853.

18. Y. Li, G. Yin, Y. Gao, T. Köhler, J. Lucaßen, and M. Schmid, "Sodium Control in Ultrathin Cu (In, Ga) Se2 Solar Cells on Transparent Back Contact for Efficiencies Beyond 12%," *Solar Energy Materials and Solar Cells* 223 (2021): 110969.

19. M. Bär, W. Bohne, J. Röhrich, et al., "Determination of the Band Gap Depth Profile of the Penternary Cu (In (1− X) GaX) (SYSe (1− Y)) 2 Chalcopyrite From Its Composition Gradient," *Journal of Applied Physics* 96, no. 7 (2004): 3857–3860.

20. Z. Gao, Y. Xiong, J. Wang, et al., "Efficiency Improvement for Post-Sulfurized CIGS Solar Cells Enabled by In Situ Na Doping," *Journal of Energy Chemistry* 101 (2025): 324–332.

21. J. Keller, S. Mudgal, N. M. Martin, O. Donzel-Gargand, and M. Edoff, "Rubidium Fluoride Absorber Treatment for Wide-Gap and Bifacial Ag (In, Ga) Se2 Solar Cells," *Solar RRL* 9, no. 16 (2025): 2500423.

22. E. Avancini, R. Carron, T. P. Weiss, et al., "Effects of Rubidium Fluoride and Potassium Fluoride Postdeposition Treatments on Cu (In, Ga) Se2 Thin Films and Solar Cell Performance," *Chemistry of Materials* 29, no. 22 (2017): 9695–9704.

23. S. Ishizuka, N. Taguchi, and P. J. Fons, "Similarities and Critical Differences in Heavy Alkali-Metal Rubidium and Cesium Effects on Chalcopyrite Cu (In, Ga) Se2 Thin-Film Solar Cells," *Journal of Physical Chemistry C* 123, no. 29 (2019): 17757–17764.

24. S. Lee, E. S. Lee, T. Y. Kim, et al., "Effect of Annealing Treatment on CdS/CIGS Thin Film Solar Cells Depending on Different CdS Deposition Temperatures," *Solar Energy Materials and Solar Cells* 141 (2015): 299–308.

25. R. Fonoll-Rubio, M. Placidi, T. Hoelscher, et al., "Characterization of the Stability of Indium Tin Oxide and Functional Layers for Semitransparent Back-Contact Applications on Cu (in, Ga) Se2 Solar Cells," *Solar RRL* 6, no. 7 (2022): 2101071.

26. C. Rath, Y. Gao, T. Koehler, and M. Schmid, "Impact of Band-Gap Gradient in Semi-Transparent and Bifacial Ultra-Thin Cu (In, Ga) Se2 Solar Cells," *Advanced Materials Interfaces* 11, no. 13 (2024): 2400085.

27. Y.-S. Son, H. Yu, J.-K. Park, et al., "Control of Structural and Electrical Properties of Indium Tin Oxide (ITO)/Cu (In, Ga) Se2 Interface for Transparent Back-Contact Applications," *Journal of Physical Chemistry C* 123, no. 3 (2019): 1635–1644.

28. S. Grover, J. V. Li, D. L. Young, P. Stradins, and H. M. Branz, "Reformulation of Solar Cell Physics to Facilitate Experimental Separation of Recombination Pathways," *Applied Physics Letters* 103, no. 9 (2013): 093502.

29. J. V. Li, S. Grover, M. A. Contreras, K. Ramanathan, D. Kuciauskas, and R. Noufi, "A Recombination Analysis of Cu (In, Ga) Se2 Solar Cells With Low and High Ga Compositions," *Solar Energy Materials and Solar Cells* 124 (2014): 143–149.

30. T. Koehler, Y. Gao, and M. Schmid, "Bifacial and Angular-Resolved Performance Characterization of Ultrathin Cu (In, Ga) Se2 Solar Cells Including Nanostructures," *Advanced Energy and Sustainability Research* 5, no. 12 (2024): 2400168.

31. D. Schmid, M. Ruckh, F. Grunwald, and H.-W. Schock, "Chalcopyrite/Defect Chalcopyrite Heterojunctions on the Basis of CuInSe2," *Journal of Applied Physics* 73, no. 6 (1993): 2902–2909.

32. S. Ishizuka and P. J. Fons, "Role of the Cu-Deficient Interface in Cu (In, Ga) Se_2 Thin-Film Photovoltaics With Alkali-Metal Doping," *Physical Review Applied* 15, no. 5 (2021): 54005.

33. M. D. Heinemann, V. Efimova, R. Klenk, et al., "Cu (In, Ga) Se2 Superstrate Solar Cells: Prospects and Limitations," *Progress in Photovoltaics: Research and Applications* 23, no. 10 (2015): 1228–1237.

34. J.-H. Yoon, J.-H. Kim, W. M. Kim, et al., "Electrical Properties of CIGS/Mo Junctions as a Function of MoSe2 Orientation and Na Doping," *Progress in Photovoltaics: Research and Applications* 22, no. 1 (2014): 90–96.

35. M. Saifullah, K. Kim, R. Shahzad, et al., "Insertion of the AGS Layer at the CIGSe/ITO Interface: A Way to Reduce the Formation of the GaOx Interfacial Phase in CIGSe Solar Cells," *Solar Energy Materials and Solar Cells* 178 (2018): 29–37.

36. Y. Li, *Sodium Doping, Back Interface Modification and Light Trapping in Bifacial Semi-Transparent Ultrathin Cu (In, Ga) Se2Solar Cells* (Universitaet Duisburg-Essen, 2022).

37. S. Puttnins, S. Levcenco, K. Schwarzburg, et al., "Effect of Sodium on Material and Device Quality in Low Temperature Deposited Cu (In, Ga) Se2," *Solar Energy Materials and Solar Cells* 119 (2013): 281–286.

38. F. Pianezzi, P. Reinhard, A. Chirilă, et al., "Unveiling the Effects of Post-Deposition Treatment With Different Alkaline Elements on the Electronic Properties of CIGS Thin Film Solar Cells," *Physical Chemistry Chemical Physics* 16, no. 19 (2014): 8843–8851.

39. S. Ishizuka, "CuGaSe2 Thin Film Solar Cells: Challenges for Developing Highly Efficient Wide-Gap Chalcopyrite Photovoltaics," *Physica Status Solidi* 216, no. 15 (2019): 1800873.

40. A. Sharan, F. P. Sabino, A. Janotti, N. Gaillard, T. Ogitsu, and J. B. Varley, "Assessing the Roles of Cu-And Ag-Deficient Layers in Chalcopyrite-Based Solar Cells Through First Principles Calculations," *Journal of Applied Physics* 127, no. 6 (2020): 065303.

Supporting Information

Additional supporting information can be found online in the Supporting Information section. **Figure S1:** (a) TEM measurement of ITO/CIGSe interface for sample preNa2Rb6_GaIn with the yellow line being the marked area for (b) the EDX measurement of Ga and O. **Figure S2:** Extraction of activation energy E_a from linear fit on temperature-dependent V_{oc} measurement for different Na and Rb variations on (a, c) Mo and (b, d) ITO substrates. **Figure S3:** Raman measurement of Na- and Rb-treated samples. At 156 cm^{-1}, the OVC peak can be faintly seen. At 178 cm^{-1}, a clear CIGSe peak is measured. **Figure S4:** Complete GDOES-depth profile with rel. absorber depth for sample of ultra-thin CIGSe with (a) 2 mg of pre–DT-Na, 6 mg of Rb; (b) 2 mg of pre–DT-Na, 6 mg of Rb, and adjusted Ga gradient; (c) 0 mg of Na, 6 mg of Rb. The absorber region is estimated to lie between the vertical lines.